48th AIAA Aerospace Sciences Meeting Including the New Horizons Forum and Aerospace Exposition
4 - 7 January 2010, Orlando, Florida

AIAA 2010-1561

Simulation of Flow Separation and Reattachment on a Re-entry Capsule Afterbody Frustum

Krishnendu Sinha* and Ayanangshu Dey†
Indian Institute of Technology Bombay, Mumbai, 400076, India.

Abstract

In this paper the flowfield around an Apollo-shaped capsule at non-zero angle of attack is numerically investigated. The focus is on the afterbody flowfield, especially the windward side. Experiments have shown that there is local flow separation and reattachment on the windward meridian at selected angles of attack. Local flow reattachment on the afterbody can lead to high surface heating. Further, the size of the windward separation bubble is found to decrease with increasing angle of attack. Simulations are performed at a fixed Mach number and varying angles of attack. The solutions reproduce all the experimentally observed flow features, including a localized separation bubble on the windward meridian. The simulations also predict the variation of the windward reattachment location with angle of attack correctly. The numerical solutions are further used to study the unsteady nature of the flow, the three-dimensional flow pattern in the near wake and its effect on the surface heat transfer rate.

I Introduction

Re-entry capsules usually consist of a blunt-faced forebody and a conical afterbody. The flow on the afterbody is characterized by a large separation bubble. The surface pressure and heating rate in the recirculation region are considerably lower than the forebody levels. However, the uncertainty in the predicted heating levels is significantly higher on the afterbody. This is primarily because of the limitations in computational approaches to simulate the separated flow accurately. Several recent efforts have attempted to predict re-entry capsule afterbody flowfield, with considerable success. Simulation of axi-symmetric and three-dimensional flowfields, both laminar and turbulent cases, reproduce in-flight measurement of heating levels well.[1,2]

Afterbody flowfields are characterized by free-shear layers enclosing recirculation bubbles with multiple vortices. At non-zero angle of attack, the separation bubble is asymmetric and is mostly confined to the leeward side. The windward flow is often attached to the conical frustum and separates only at the base. Schneider[3] presents a comprehensive survey of flight and ground-test data relevant to afterbody flowfield. In some cases, the windward flow may separate at the beginning of the afterbody and then reattach along the frustum. Fig. 1 shows a typical flowfield where the windward free shear layer can be seen to curve around and reattach on the conical frustum. A reattachment shock is generated at this location. The attached flow subsequently separates at the base. On the leeward side, the flow separates at the shoulder to form the large recirculation region. The recompression shock waves and the following unsteady wake is clearly visible in the shadowgraph.

Reattachment of the separated shear layer is often marked by high local pressure and heat transfer. The magnitude and location of the reattachment point may therefore be of interest for the afterbody heatshield design. Kruse *et al.*[4] show that the reattachment location is dependent on the freestream Mach number, angle of attack, and whether the flow is laminar or turbulent. They conducted tests on an Apollo-shaped body flying at different Mach numbers and angles of attack. Figure 2 taken from Ref. 4 identify the test cases on a Mach number vs. angle of attack plot. Each case is marked based on whether the flow is separated or attached on the windward afterbody. For a given Mach number, as the angle of attack increases, the windward afterbody flow changes from fully separated to partially attached, and finally to completely attached along the frustum. The percentage of the windward meridian covered by attached flow (marked on the data points in Fig. 2) is found to increase with angle of attack. The separation point is generally anchored close to

*Assistant Professor, Department of Aerospace Engineering, AIAA Member.
†Senior Undergraduate, Department of Aerospace Engineering

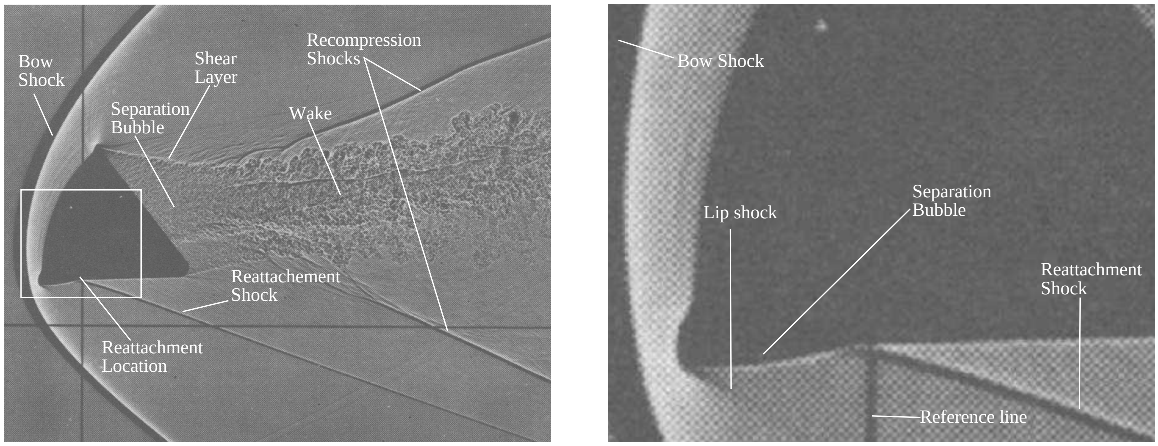

(a) (b)

Figure 1: Experimental shadowgraph (a) depicting salient features in the flow around an Apollo- shaped body at Mach 2.2 and angle of attack of 25 deg. (adapted from Kruse *et al.*[4]). A magnified view of the windward separation bubble is shown in (b)

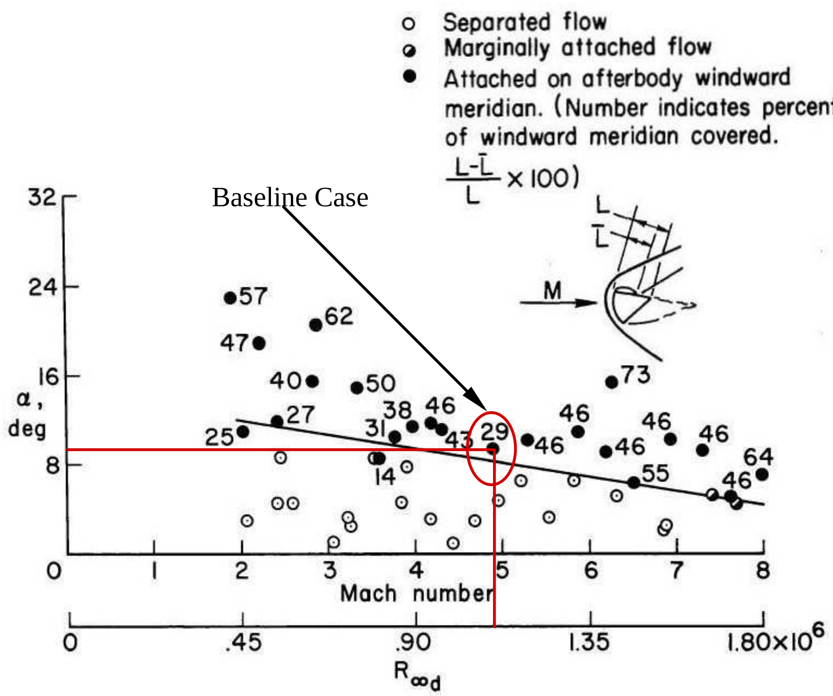

Figure 2: Experimental observation of flow separation and attachment on the afterbody windward meridian is identified for different Mach number and angle of attack conditions (reproduced from Ref. 4).

the shoulder. The reattachment point therefore shifts upstream along the frustum as the angle of attack increases.

To the best of our knowledge the flowfields observed by Kruse *et al.*[4] have not been analyzed using modern CFD. Specifically, the capability of numerical simulations to reproduce the local separation and reattachment locations on the windward afterbody needs to be evaluated. This is the objective of the current work, where both qualitative and quantitative comparison between CFD and experiments is presented. The CFD solution is further used to complement the experimental observations. Specifically, the three-dimensional flow structure on the afterbody is studied in detail and its effect on the surface properties is discussed. Also the unsteady nature of the afterbody flow, especially along the windward meridian, is characterized using the simulation results.

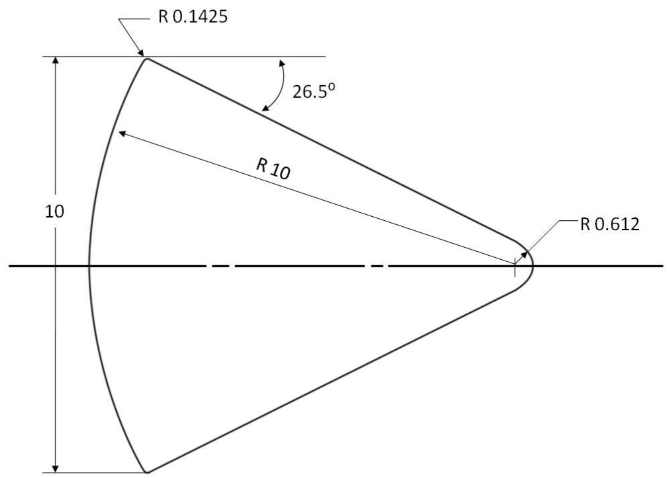

Figure 3: Outer mold line used for the current simulations. All dimensions are in mm.

Free-stream Conditions	
M_∞	4.9
ρ_∞ (kg/m^3)	1.1827
U_∞ (m/s)	1697
T_∞ (K)	298.5
P_∞ (N/m^2)	101325
T_{wall} (K)	298.5
Re_D	1.09×10^6
α (degree)	10

Table 1: Free-stream and wall boundary conditions for the baseline simulation

The capsule geometry used by Kruse *et al.*[4] is chosen for simulation at different angles of attack for a fixed Mach number. Details of the configuration are given in section II, followed by a description of the simulation methodology in section III. Numerical simulation of these configurations can be challenging, owing to the high degree of three dimensionality of the flow field. Capturing the prominent flow features like the free shear layer on the leeward side and the local flow separation and reattachment on the windward side will pose significant difficulty in designing a grid that will provide an accurate solution. Flow field computed at a representative set of conditions is presented in section IV. The numerical solutions exhibit all the salient features, including the windward separation bubble, identified in the experimental shadowgraph (see Fig. 1). A comparison of the computed reattachment location along the windward meridian with the experimental data is presented at the end.

II Configuration

The experimental model is an Apollo-shaped capsule with a spherical forebody and a conical afterbody, and is used to define the outer mold line for the simulation (see Fig. 3). The forebody radius is equal to the body diameter of 10 mm. The afterbody cone has a 26.5 deg half angle and a spherical base. The base radius is specified to be 1 mm, with a center of curvature matching that of the forebody surface. This, however, results in a slope discontinuity between the conical frustum and the spherical base. In order to satisfy the tangency condition, the base radius is modified to 0.612 mm. Also, the corner between the forebody and afterbody is rounded off with a radius of 0.1425 mm. No geometrical information has been provided about this corner in the original reference.[4]

We choose the freestream conditions corresponding to the experimental data point marked in Fig. 2. For this case the free-stream Mach number is 4.9 and Reynolds number based on the freestream conditions and the body diameter is 1.09×10^6. Pressure in the experimental facility is noted to be 1 atm. The remaining freestream parameters are calculated to match the above values, and they are listed in Table 1. The angle of attack for the selected test case is close to 10°. Baseline simulations are performed at this angle of attack to study the flowfield in detail. Additional cases are computed for α varying systematically in the range from 8° to 14°, with other freestream parameters unchanged. The flowfield solutions are compared to study the variation of the windward reattachment location with angle of attack. As per the experimental data presented in Fig. 2, a lower value of α moves the reattachment point downstream. This results in attached flow over a smaller fraction of the windward meridian. On the other hand, the reattachment location shifts upstream at higher angles of attack, leading to a smaller separation bubble on the windward side and a large region of attached flow on the frustum.

In the work of Kruse *et al.*[4] a considerable amount of effort is devoted to identify the laminar and turbulent regions in the flow around the Apollo-shaped body. The transition location is correlated with the Reynolds number based on post-shock conditions (density, velocity and viscosity), denoted by subscript 2. The arc length measured from the nose stagnation point to the shoulder, denoted by x, is used to define the Reynolds number Re_{2x} . Experimental data shows that the flow transitions at the shoulder for Re_{2x} in the range of 2.5×10^5 to 3.5×10^5 . For higher values of Re_{2x} there is turbulent flow on the afterbody, whereas for lower values some region of laminar flow is observed downstream of the corner. For the baseline case considered in this work, Re_{2x} is 0.91×10^5 at the windward shoulder. Therefore a part of the shear layer originating at this point is expected to be laminar. The flow may transition further down on the windward meridian. At the leeward shoulder Re_{2x} is 2.9×10^5. This is in the range of transitional flow noted above. Therefore there are higher chances of the flow on the leeward afterbody to be turbulent. The simulations presented in this work assume laminar flow, which is true for the forebody as well as part of the afterbody. Effect of turbulence is neglected in the simulations, so as to eliminate the uncertainties involved in modeling of transition/turbulence.

III Simulation Methodology

The flow field around the re-entry configuration is simulated by solving the three-dimensional Navier-Stokes equations. The working medium, air, is taken as a perfect gas with molecular weight of 28.96 grams/mole and ratio of specific heat γ equal to 1.4. The temperature dependence of molecular viscosity is as per Sutherlands law, and the conductivity is calculated using a Prandtl number of 0.72. Effect of turbulence on the flow is neglected as per the discussion above. Part of the laminar wake is found to be unsteady, and time-averaged solutions are computed for comparison with experimental data.

The numerical method uses a modified (low dissipation) form of Steger-Warming flux vector splitting approach[5] for evaluating the convective fluxes. Central differencing is used for the viscous fluxes, and the code is implemented in parallel using the Message Passing Interface.[6] The code has been systematically validated for flat plate boundary layers and blunt body flows. An axi-symmetric version of the code has also been applied to a re-entry capsule configuration.[2]

The numerical method is second-order accurate in space and time. An implicit full matrix Data-Parallel Lower-Upper Relaxation method[7] is used to integrate the equations in time. The method involves Newton sub-iterations to converge the L_1 norm of the density residual to a prescribed tolerance, taken to be 10^{-5} of a characteristic density in the flow. First-order backward Euler time-integration is also implemented in the code and is mainly used to integrate through the initial transient flow development. A similar method is used in the three-dimensional unsteady computation of the Fire II re-entry capsule presented in Refs. 8 and 9.

A. Grid Generation

The three-dimensional volume grid used in the computation consists of six grid blocks with one-to-one grid point matching at the inter-block boundaries. The block topology is shown in Figs. 4 and 5. Blocks II, III and V are axi-symmetric, whereas I, IV and VI are non-axisymmetric to avoid grid singularity at the nose and base of the vehicle. The outer boundary encloses the bow shock and extends upto about 4.5 diameters downstream of the vehicle. The flow at the exit boundary is supersonic and is not expected to influence the flowfield near the vehicle. The flow around the Apollo-shaped capsule at non-zero angle of attack is not axi-symmetric. Specifically, the bow shock and the wake are skewed towards the leeward side with partly

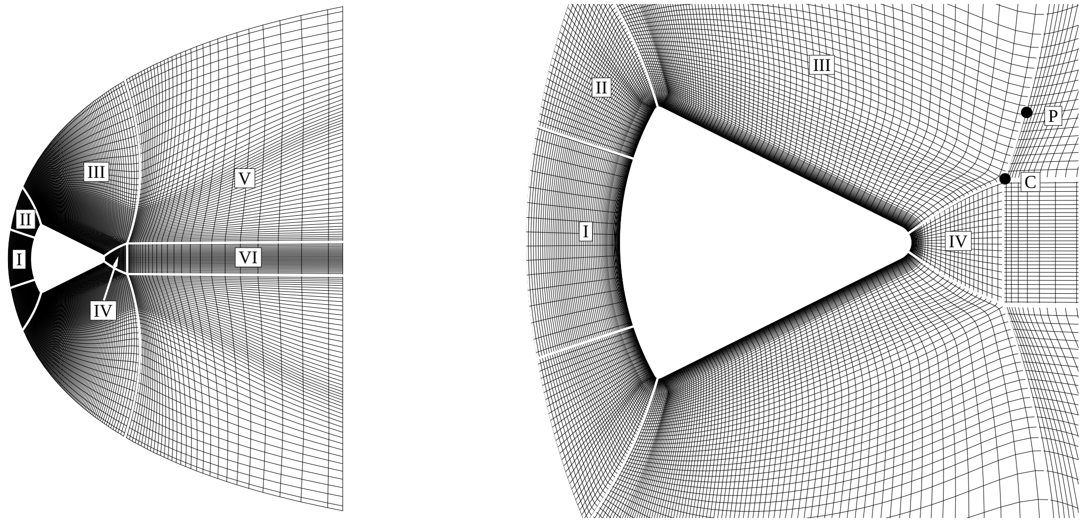

(a) (b)

Figure 4: Multi-block grid topology on the pitch-plane showing the (a) overall grid and (b) a magnified view (every second point is shown in each direction) White lines correspond to the block boundaries.

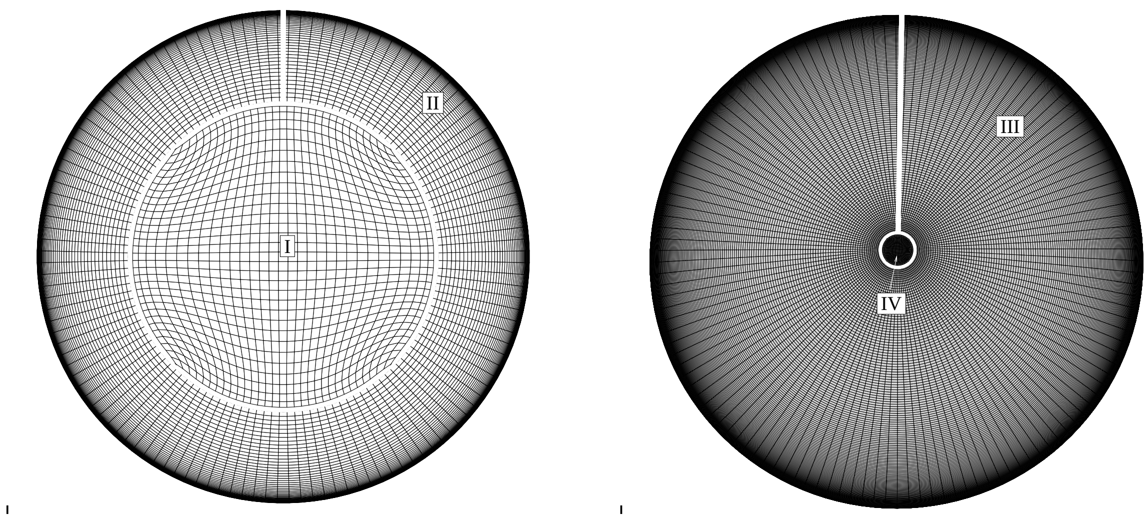

(a) (b)

Figure 5: Grid topology on the body surface: (a) forebody and (b) afterbody and base. White lines correspond to the block boundaries.

Block No.	$i \times j \times k$
I	$33 \times 33 \times 171$
II	$55 \times 129 \times 171$
III	$164 \times 129 \times 171$
IV	$33 \times 33 \times 120$
V	$31 \times 129 \times 52$
VI	$33 \times 33 \times 31$

Table 2: Grid dimensions in each block of the three-dimensional volume grid

attached flow on the windward afterbody. A non-axisymmetric block topology may be more appropriate in such a case. We have used the current axi-symmetric topology shown in Figs. 4 and 5 because of convenience in grid generation and refinement. However control points are placed along the block boundaries (as discussed

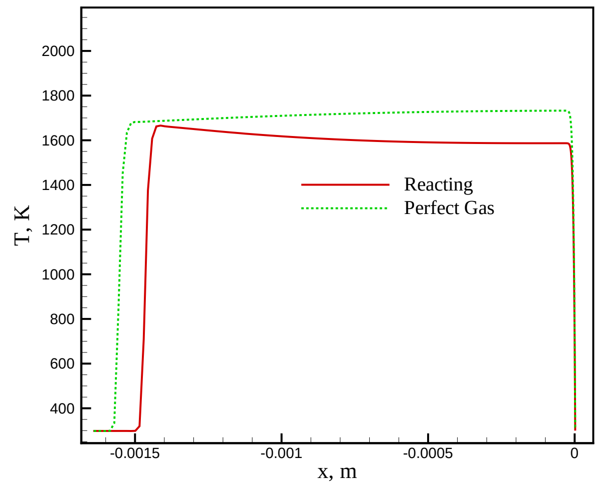

Figure 6: Comparison of temperature along stagnation streamline computed using perfect gas and reacting simulation at the baseline conditions.

below) to tailor the grid to the asymmetric flow features.

The forebody of the vehicles is spanned by grid blocks I and II. The primary objective is to resolve the boundary layer and bow shock accurately. A layer of orthogonal grid cells is extruded from the body surface to span the boundary layer region. The first cell center is at a distance of 1×10^{-6}m from the wall and the grid is exponentially stretched in the wall normal direction. The grid is also refined in the vicinity of the shock wave to capture the flow gradients accurately. In the wall parallel direction the grid points are clustered in the shoulder expansion region.

The afterbody flowfield is of primary interest in this work. Special attention is given to the design of the grid in the near wake. On the windward side, the flow separates at the shoulder forming a small localized separation bubble, attaches at about halfway along the frustum and separates again at the base. The i-direction grid along the conical frustum is therefore refined at the shoulder and the base corners. A control point is placed at the expected reattachment location for carefully monitoring and refining the grid in this region. A shear layer is formed that encloses the localized recirculation bubble. The extrusion layer consisting of orthogonal cells is extended from the surface to a height that envelops the shear layer so that it is reproduced accurately. On the leeward side the flow separates at the shoulder to form a large unsteady recirculation bubble. This is spanned mostly by grid block III, and control points are placed along the downstream boundary of the grid block to tailor the grid to the dominant flow structure. A large number of points are clustered in the unsteady near wake so as to capture the flow features well. The outer flow is inviscid and the grid there is relatively coarse. Special attention is given to the free shear layer that encloses the separation bubble. A control point P is placed appropriately to align the grid to the free shear layer and to cluster enough points to resolve it accurately. In the circumferential j-direction there is no apriori knowledge of the flow gradients. Therefore the grid points are distributed uniformly in this direction.

Grid blocks IV and VI cover the base region. The wall normal grid is constrained to an initial spacing of 1×10^{-6} m. The grid is also refined near the triple point C and then stretched exponentially to the exit boundary. The outer block V spans the far wake and also the inviscid flow outside the wake including the recompression shock. The total number of grid points in i, j and k directions in each block is listed in Table 2. Overall, there are 5.4×10^6 grid points and they are computed in parallel on 28 processor cores of a xeon-based machines.

B. High temperature effects

At the chosen free-stream conditions the post-shock temperature predicted by normal shock relations with perfect gas assumption is 1674 K. At this temperature the effect of vibrational excitation and possible chemical dissociation reactions on the computed flowfied needs to be assessed. This is done by comparing the perfect gas solution with that obtained from a chemically reacting simulation. In the latter case, air is modeled as a neutral mixture of five species (N_2, O_2, NO, N and O), with five finite rate chemical reactions. Thermal non-equilibrium effects are considered by solving a separate transport equation for the mixture

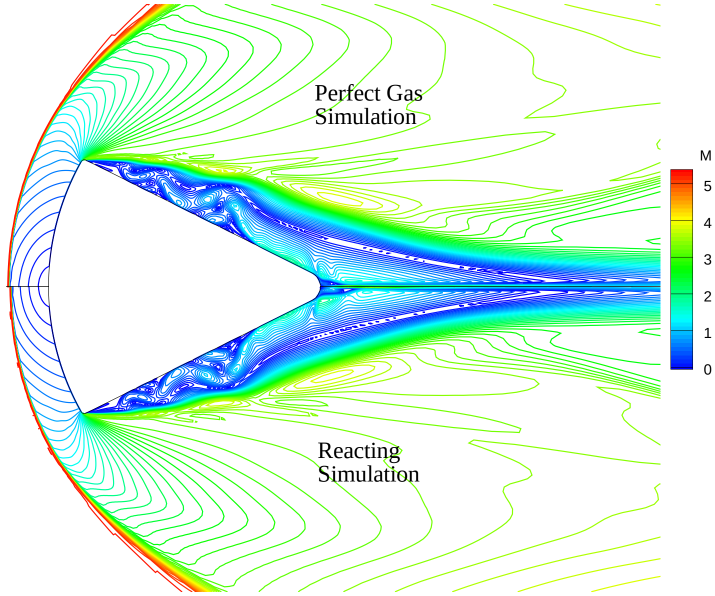

Figure 7: Mach Number contours comparing perfect gas and reacting simulations of the flow around the Apollo-shaped body at zero angle of attack.

vibrational energy, similar to that used in Ref. 2. Axi-symmetric simulations for $\alpha = 0°$ is considered for simplicity.

The chemically reacting solution computed at the baseline conditions reported above shows vibrational excitation in the post-shock region resulting in a lower temperature downstream of the bow shock (see Fig. 6). The translational and vibrational temperatures are found to be lower by upto 150 K compared to the perfect gas temperature along the stagnation streamline. The bow shock standoff distance is reduced by about 5.5% of the body diameter due to the high-temperature effect. No dissociation is observed in the solution and the mass fractions of N_2 and O_2 remain at their freestream values throughout the flowfield. Figure 7 shows the Mach number contours in the solution computed using the two approaches. There is negligible difference in the afterbody flowfield between the two cases. The shape of the shear layer and the flow pattern in the recirculation bubble, although unsteady, follow the same pattern in the perfect gas and chemically reacting solution. This maybe because of the flow expansion around the shoulder, which cools the gas and reduces vibrational excitation effects drastically. Thus the effect of high-temperature phenomena on the flowfield at the chosen freestream conditions is negligible. This is especially true for the afterbody flow, which is the focus of the current study.

IV Results

The flowfield around the Apollo-shaped body is initialized to free-stream values all over the domain except for a small region near the base. As the simulation progresses the bow shock and the boundary layer on the vehicle are formed, followed by flow separation on the afterbody. As the separation bubble forms on the windward side, the reattachment location is found to show large oscillations along the afterbody frustum. A first order time integration is used to go past this initial transient, until the point when the reattachment point oscillations are stabilized. A second-order time accurate simulation is used thereafter and data is collected over a period of time to compute the time-averaged flowfield. The location of the windward attachment point is found to converge over an averaging time of 60-70 t_{flow}, where t_{flow} is defined in terms of the free-stream velocity and the body diameter. By comparison, the leeward separation bubble requires much longer time averaging to arrive at a converged solution. The time-averaged results presented below correspond to an averaging time duration of about 400 t_{flow}. Some residual asymmetry in the afterbody surface streamlines is observed on the leeward side. The time-averaged flowfield is expected to be symmetric about the pitch plane if data is collected over a longer time period.

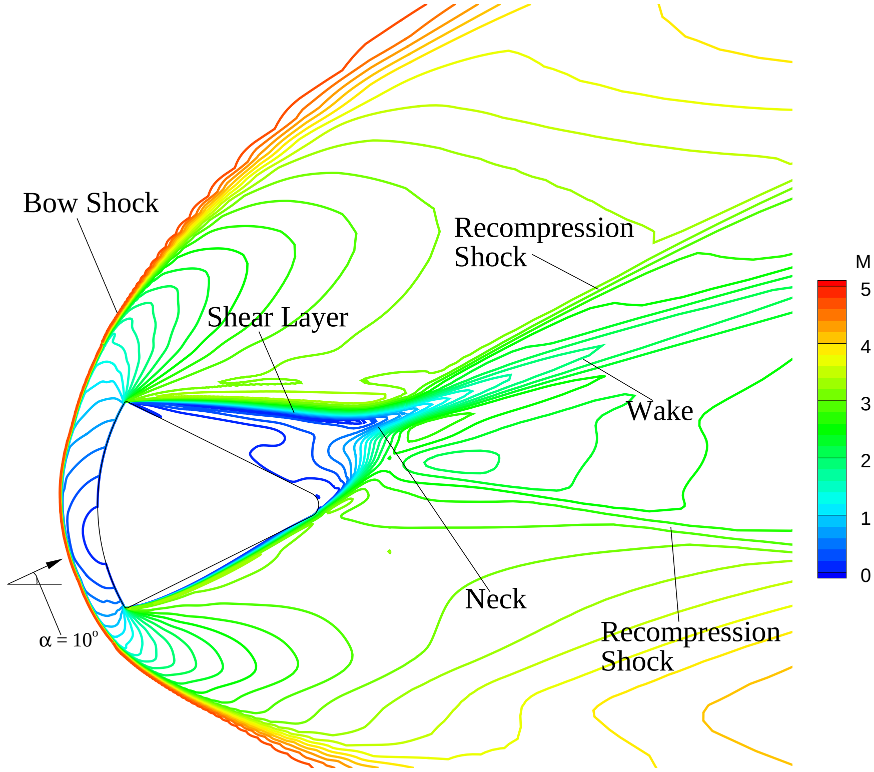

Figure 8: Mach number distribution in the pitch plane showing the prominent features in the time-averaged flowfield. The freestream flow is from lower left side with an angle of attack of 10°.

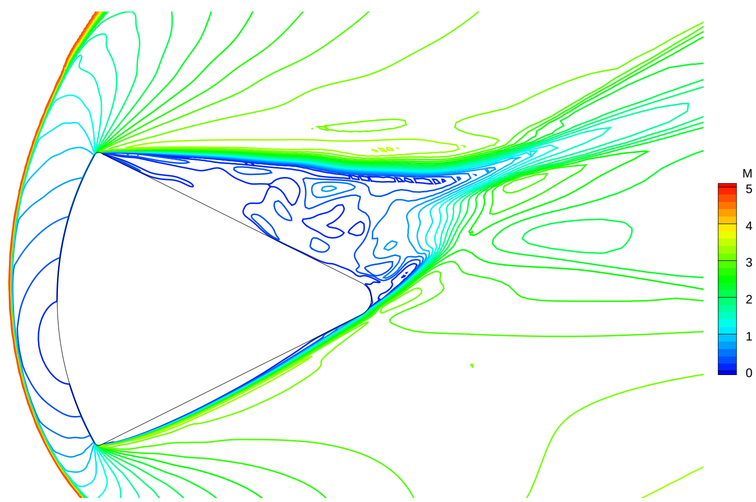

Figure 9: A magnified view of the instantaneous flowfield near the body in terms of the Mach number distribution in the pitch plane

A. Baseline simulation

The Mach number distribution of the baseline configuration in the pitch plane is presented in Fig. 8. The data corresponds to the time-averaged flowfield. The main flow features include the bow shock in front of the vehicle, which is asymmetric about the body axis because of a 10° angle of attack. The post shock flow on the forebody is subsonic with Mach number reaching one just before the shoulder. Flow expansion around the shoulder results in Mach number of about 3.2 on the leeward side in the inviscid region outside the wake. On the windward side the Mach number is around 3.1. The boundary layer separates immediately after

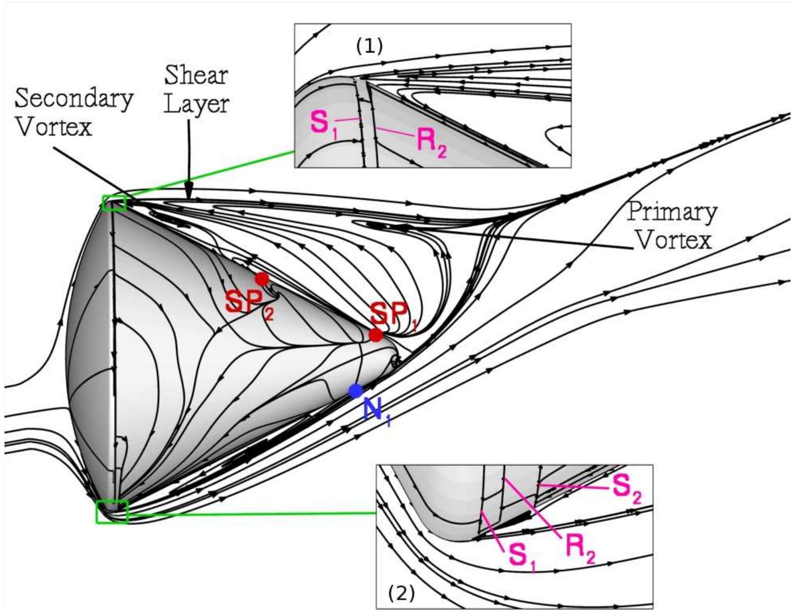

Figure 10: Representative streamlines are plotted in the pitch plane and the body surface to visualize the near-wake flowfield. Insets (1) and (2) show magnified view of the leeward and windward corners respectively.

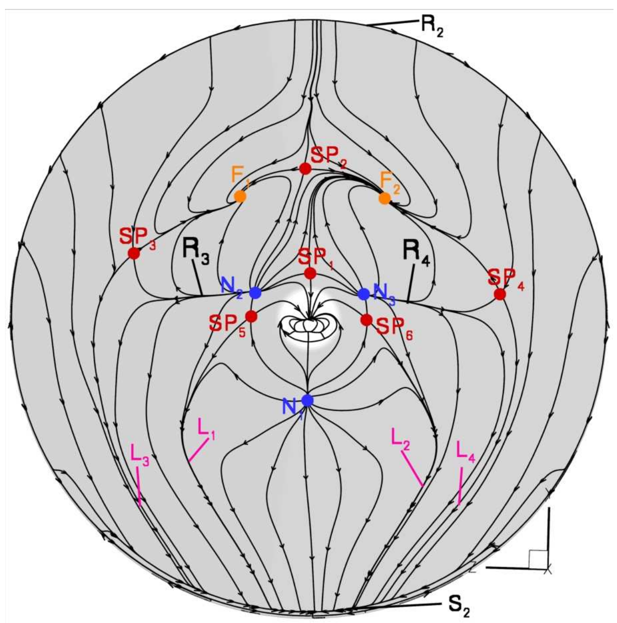

Figure 11: Surface flow pattern on the afterbody highlighting limiting streamlines and critical points for $\alpha = 10^{\circ}$

the shoulder to form a small separation bubble on the windward afterbody. A large recirculation bubble is formed on the leeward side and the shear layer enclosing the separation bubble coalesces at the neck, where the recompression shock is formed. The flow in the recirculation bubble is mostly subsonic and the Mach number exceeds one at the neck. The flow in the far wake downstream of the neck is mostly supersonic.

Figure 9 shows a magnified view of the flowfield in the vicinity of the vehicle. The data here corresponds to a single time realization of the flowfield to highlight its unsteadiness. Majority of the unsteadiness is confined to the leeward recirculation bubble. The shear layer enclosing the separation region, the far wake and the recompression shocks show small variations with time. On the windward side the reattachment location on the meridian of the afterbody frustum oscillates about a mean location. The inviscid flow outside the wake

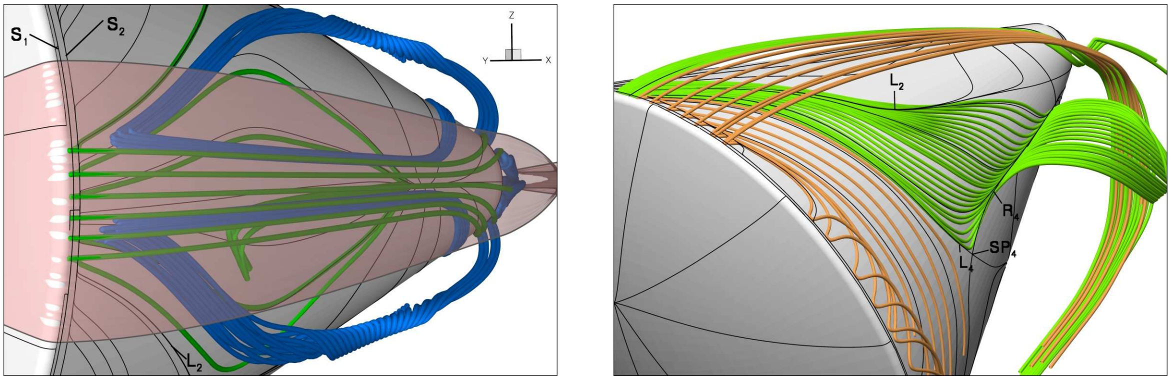

(a) (b)

Figure 12: Representative volume streamlines are drawn on the windward afterbody to study the three-dimensional flow pattern (a)inside and (b)outside the windward separation bubble

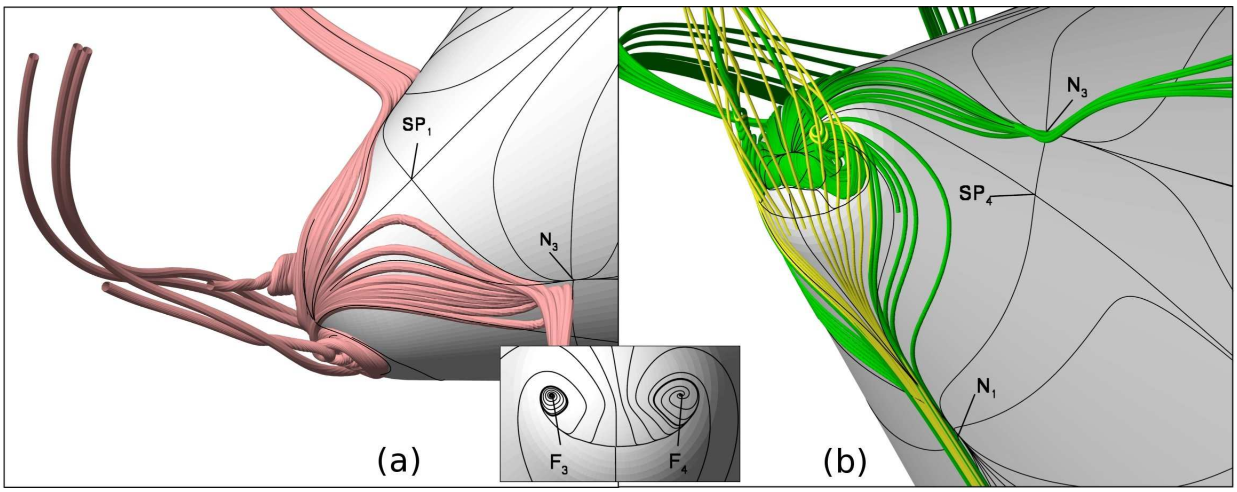

Figure 13: Three-dimensional flow in the vicinity of the base: (a)windward and (b)leeward side depicted via volume streamlines.

and flow on the forebody is found to be steady. In the subsequent paragraphs the time-averaged solution is presented in detail and the three-dimensional flow structures in the recirculation bubble, both on the windward and leeward sides, is studied carefully.

The near wake flow pattern is visualized in terms of streamlines plotted on the symmetry plan and the body surface (Fig. 10). On the leeward side two main vortical structures are observed; a primary vortex near the shear layer and a smaller secondary vortex near the wall. The flow enters the symmetry plane from a point on the afterbody surface near the base, denoted by SP_1. A part of the flow goes into the primary vortex and exits into the far wake along the shear layer. The other part goes into the secondary vortex and exits the symmetry plane along the afterbody surface at the point SP_2. A magnified view of the shoulder region of the leeward symmetry plane is shown in inset (1),where the points of primary separation and secondary reattachment are clearly visible. The corresponding surface streamlines are denoted by S_1 and R_2 respectively. On the windward side the flow separates at the shoulder to form an elongated recirculation bubble. The shear layer that originates at the primary separation S_1 goes on to attach downstream on the afterbody frustum. A node of attachment is formed, denoted by N_1, and we see flow reversal on the afterbody surface upstream of this point. A small secondary vortex is observed near the shoulder (see inset (2) in Fig. 10), with separation and reattachment along S_2 and R_2 respectively.

The surface streamlines on the afterbody(Fig. 11) shows an interesting pattern of limiting streamlines and critical points. These play a key role in understanding the three-dimensional flow in the recirculation bubble. Lines of divergence (R_3 and R_4, for instance) correspond to local flow attachment on the surface and lines of convergence, like S_2, denote local flow separation. The critical points correspond to regions where

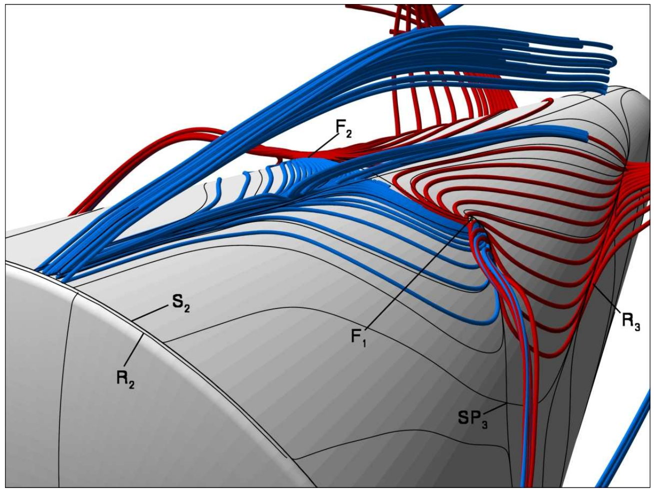

Figure 14: Three-dimensional flow in the leeward recirculation bubble elucidated via representative volume streamlines.

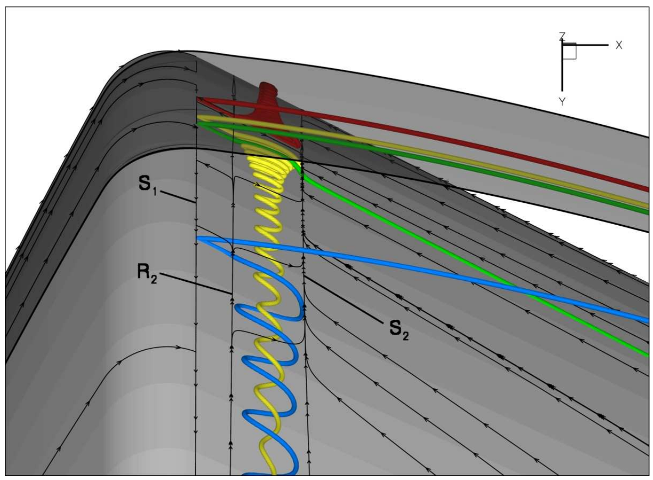

Figure 15: Three-dimensional structure of the secondary vortex formed at the windward shoulder

the shear stress goes to zero. There are three kinds of critical points – node, saddle point and focus, which are denoted by N, SP and F respectively. On the leeward side the line R_2 corresponds to the secondary separation and SP_1 and SP_2 are saddle points close to the plane of symmetry. Two foci F_1 and F_2 appear on each side of the symmetry plane and the surface flow swirls into these points. On the windward side the node of attachment N_1 has streamlines diverging out of it. Some of these streamlines flow towards the shoulder and separate at S_2. Other part of the reattaching flow goes down to the base. The lines L_1 and L_2 on either side of the symmetry plane identify the extent of the windward recirculation bubble. Two additional nodes of attachment N_2 and N_3 are formed on the leeward side and part of the flow attaching at these points flow towards the base.

The three-dimensional flow structure on the windward side of the afterbody is explained in terms of the volume streamlines presented in Fig. 12(a) The blue lines show two vortical patterns, one on each side of the symmetry plane, which are followed by flow attachment on the surface. The streamlines then flow upstream and separate near the shoulder. The separated flow reattaches on the surface in the vicinity of the node N_1 and travel along the body surface towards the base. The stream surface plotted in Fig. 12(a) (pink colored) correspond to the flow separating along the primary separation line S_1 at the windward shoulder. These streamlines flow over the recirculation bubble and go on to envelop the vortical structure formed at the base. Figure 12(b) shows the surface flow pattern outside the lines L_1 and L_2, which mark the boundaries of the windward separation bubble (see Fig. 11). Flow attaching on the surface along lines R_3 and R_4 traverses upstream between the lines L_2 and L_4 towards the shoulder and separates at S_2. A similar pattern is seen

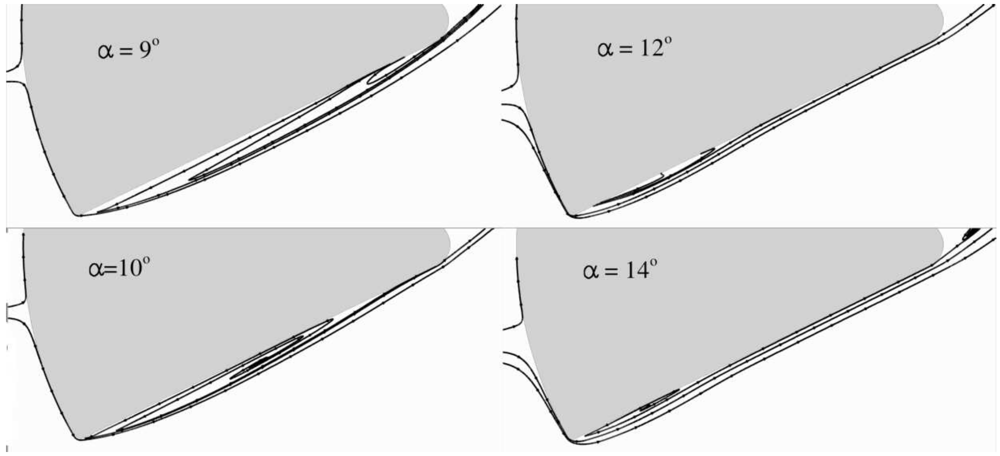

Figure 16: Windward separation bubble at various angles of attack as seen via streamlines plotted on the symmetry plane

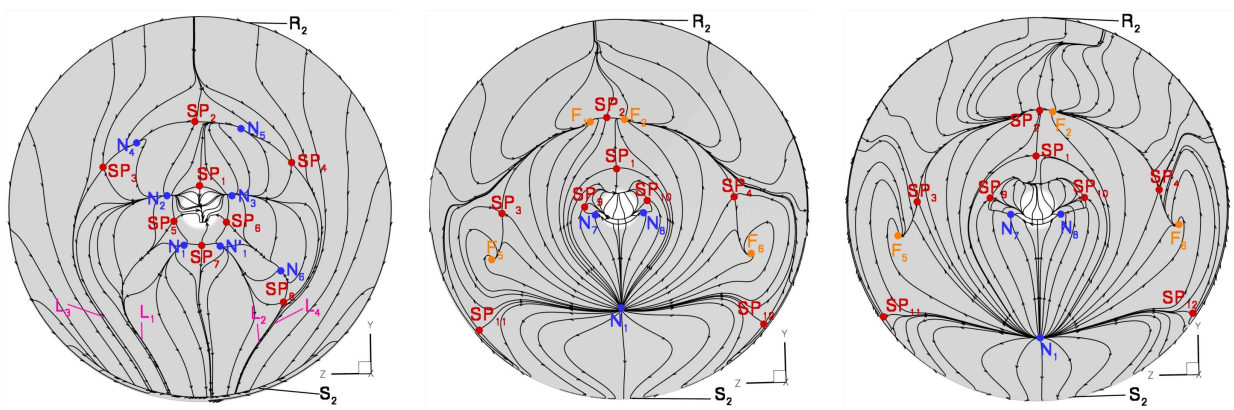

(a) (b) (c)

Figure 17: Surface flow pattern on vehicle afterbody highlighting limiting streamlines and critical points for different angles of attack: (a) 9°, (b) 12° and (c) 14°

between L_1 and L_3 on the other side of the symmetry plane.

The flow in the vicinity of the base is depicted in terms of volume streamlines presented in Fig. 13. On the leeward side the streamlines attaching on the surface at nodes N_2 and N_3 flow along the surface to the base where they get ejected through the two foci F_3 and F_4. These foci are observed (see inset in Fig. 13) at a height of 0.01 mm. from the body surface. They are not present in the surface streamline pattern shown in Fig. 11. On the windward side the flow attaching at the node N_1 curve around on the surface again to reach the base, where they are ejected into the wake. The other set of volume streamlines (yellow) originate from the primary separation point on the windward shoulder and go on to envelop the two vortical structures emanating from the base foci. The leeward flowfield is elucidated in Fig. 14 which shows that the secondary flow attaching along R_2 at the shoulder (blue streamlines) follows a spiral path on the surface to reach the focus F_1. Also, the flow attaching along R_3 (red streamlines) spirals into the focal point and all these streamlines get ejected off the surface at F_1. A similar pattern is formed on the other side of the symmetry plane at the point F_2. Figure 15 shows the secondary vortex structure on the windward afterbody. This elongated vortex runs between the lines S_2 and R_2 along much of the windward circumference. At some point the flow from the secondary vortex gets ejected into the primary structure that forms on the windward afterbody.

B. Angle of Attack variation

Simulations are performed at angles of attack varying between 8 and 14 degrees at intervals of 1 degree. Results are presented for selected cases ($\alpha = 9°$, $12°$ and $14°$) which are compared with the baseline simulation ($\alpha = 10°$) presented above. The trends in the afterbody flowfield, especially the windward side, with variation in angle of attack is presented below.

Figure 16 shows the flow along the windward meridian in terms of representative streamlines plotted on the symmetry plane. In all cases the flow separates at the shoulder and attaches downstream on the afterbody frustum. The location of reattachment moves upstream with increasing angle of attack. For $\alpha = 9°$ the separation bubble covers the conical frustum almost entirely with attachment close to the base, whereas for $\alpha = 14°$ the separation bubble is confined to a small region near the shoulder with attached flow along the rest of the afterbody frustum.

The time-averaged surface flow pattern on the afterbody frustum and base computed for different angles of attack is presented in Fig. 17. The results are compared with the baseline $\alpha = 10°$ case presented above. At $\alpha = 9°$ the surface streamline pattern shows similarity to the baseline case. On the leeward side the saddle points SP_1 through SP_4 retain their relative position. The two foci F_1 and F_2 seen earlier are replaced by nodes of separation N_4 and N_5. The streamline pattern observed at the base for $\alpha = 10°$ is somewhat reduced in size at the lower angle of attack. As a consequence the nodes of attachment N_2 and N_3 and saddle points SP_5 and SP_6 are placed closer to the base for $\alpha = 9°$. On the windward side there are two nodes of attachment N_1 and N_1' separated by a saddle point SP_7. By comparison $\alpha = 10°$ case has a single node of attachment on the windward meridian. An additional node-saddle pair (N_6 and SP_8) is formed on the right side of the symmetry plane. A similar pair is expected to appear on the left side. This asymmetry is probably because of inadequate time-averaging duration used in the computation. The lines L_1 and L_2 identify the spanwise extent of the windward separation bubble and their location is found to be comparable to that observed in the $\alpha = 10°$ case.

At an angle of attack of 12° the node of attachment N_1 along the windward meridian is shifted down towards the shoulder. This reduces the streamwise extent of the separation bubble (compared to $\alpha = 10°$). The spanwise dimension of the windward separation bubble however is noticeably increased at higherα. A pair of flow separation foci (F_5 and F_6) and saddle points SP_{11} and SP_{12} appear on the windward afterbody. On the leeward side the relative position of the saddle points SP_1 through SP_4 match the baseline case. The foci F_1 and F_2 move closer to the symmetry plane and are greatly reduced in strength compared to $\alpha = 10°$. The nodes of attachment N_2 and N_3 along with the saddle points SP_5 and SP_6 (observed at $\alpha = 10°$) disappear at higher angle of attack. The secondary separation structure at the base is larger in this case compared to $\alpha = 10°$. A new pair of nodes of separation (N_7 and N_8) and saddle points (SP_9 and SP_{10}) appear in this region. At the highest angle of attack $\alpha = 14°$, the afterbody surface flow pattern is very similar to that observed at $\alpha = 12°$, with only minor variations in the location of the critical points. The focus F_1 on the leeward side is not easily discernable at $\alpha = 14°$. The secondary separation structure observed at the base is further increased in size when compared with the other solutions. On the windward side the node of attachment N_2 moves closer to the shoulder. The saddle points SP_{11} and SP_{12} move outward. These saddle points mark the lateral extent of the windward separation bubble. Thus increasing the angle of attack decreases the streamwise extent of the windward separation bubble, but increases its spanwise dimension.

C. Surface Heat Transfer

Figure 18 shows the afterbody surface heat transfer rate computed using the time-averaged flowfield solution for the different angles of attack cases. For the baseline case $\alpha = 10°$ (Fig. 18(b)) a majority of the afterbody surface has low heat transfer rate corresponding to locally separated flow. There are three hot spots in the vicinity of the base. On the leeward side these correspond to the nodes of attachment N_2 and N_3, and on the windward side the attached flow region between the node N_1 and the base has high heat transfer rate. Flow separation at the base results in comparatively lower heating rates, whereas there is high heat transfer along the leeward shoulder corresponding to the reattachment line R_2. A similar pattern is observed for $\alpha = 9°$, where the leeward nodes of attachment result in higher localized heating than the $\alpha = 10°$ case. For higher angles of attack ($\alpha = 12°$ and $14°$), the windward nodes of attachment, and the corresponding hot spots disappear. Instead regions of low heating on the leeward frustum close to the base, which correspond to the nodes of separation N_7 and N_8 seen in Fig. 17. The high heating rate on the windward afterbody close to the base is present in all the cases simulated.

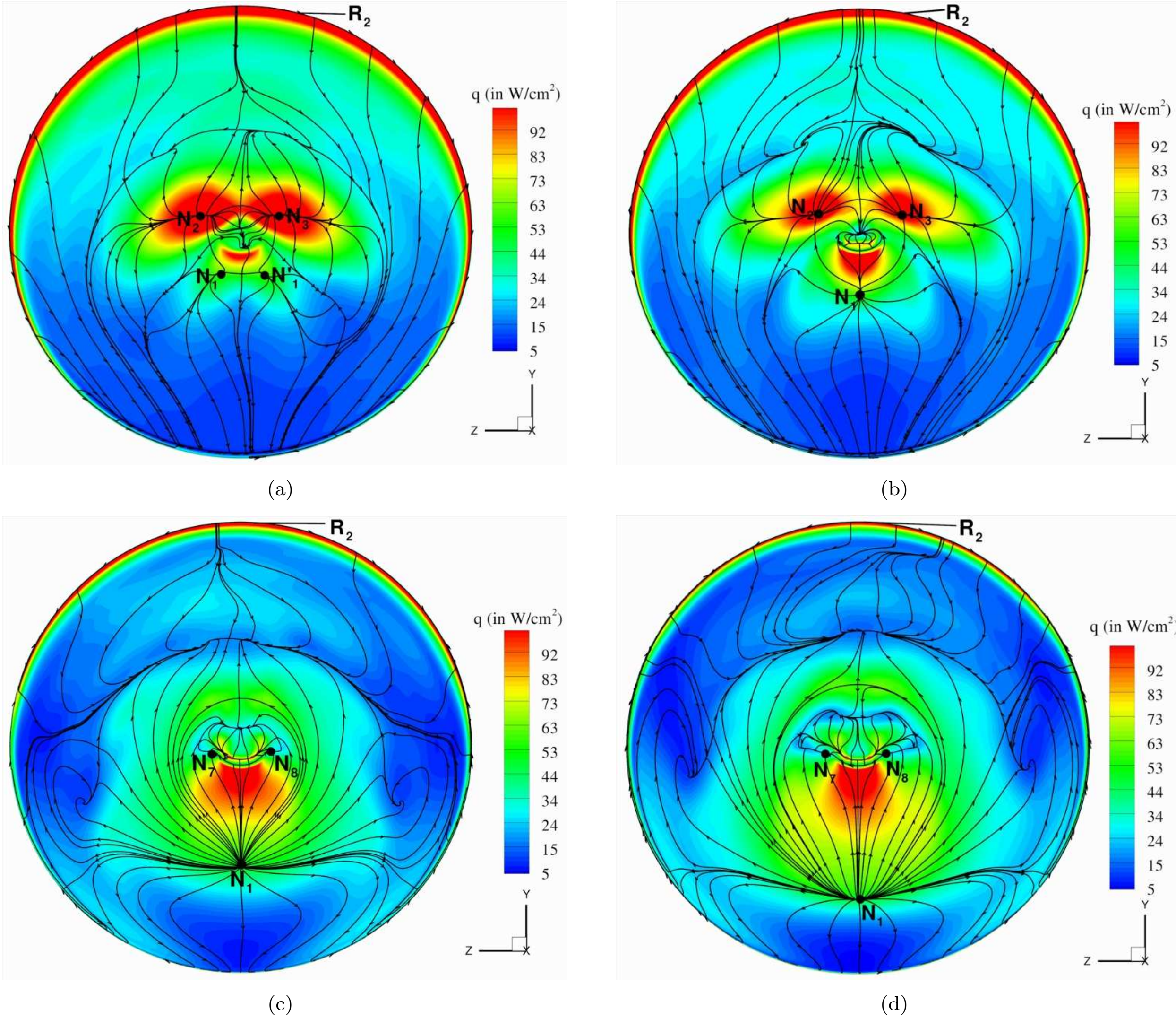

Figure 18: Surface heat transfer rate on vehicle afterbody overlaid with limiting streamlines and some critical points for different angles of attack: (a)9°, (b)10°, (c)12° and (d)14°

D. Comparison with experiments

A quantitative comparison between the CFD results and experimental data is attempted in Fig. 19 which presents the Mach Number vs α plot reproduced from Ref. **??**. The different angle of attack cases computed in the current work are plotted along the vertical line corresponding to Mach number of 4.9. The experimental data points span over a range of Mach number and alpha values. The fraction of the afterbody windward meridian that is covered by attached flow $((L-\overline{L})/L \times 100)$ is marked against each datapoint. Here $(\overline{L})$ is the distance from the shoulder to the windward node of attachment N_1 and L is taken as the total slant length of the afterbody frustum excluding the curved portion at the shoulder and base. In the experiments the location of reattachment point on the windward afterbody cannot be observed directly. The position of the reattachment shock is probably used to infer the reattachment location. The reattachment shock is not clearly visible in the CFD solutions except for the highest angle of attack case. For $\alpha = 14°$ the reattachment shock is extrapolated to the surface and is found to match the location of reattachment node closely. For the baseline case $\alpha = 10°$ the computed time-averaged solution shows that only 17% of the afterbody windward meridian lies downstream of the node of attachment whereas experiments report a value of 29% for this case. The attachment node location for $\alpha = 11°$ results in a 30% windward meridian covered with attached flow. This matches the experimental value of 29% closely. The attachment node location is found to be sensitive to the angle of attack. A change of 1° in α results in upto 13% variation in the node location. Note that $\alpha = 8°$ case shows marginally attached flow along the windward meridian, and this is found to match well with the line in Fig. 19 that separates experimentally observed separated and attached flow along the afterbody

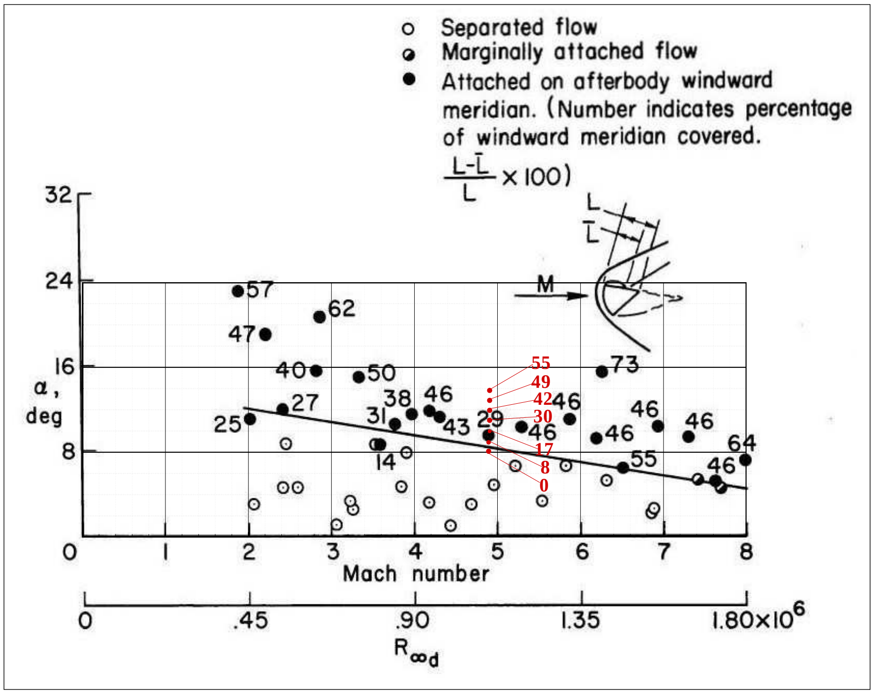

Figure 19: Mach number vs. angle of attack plot showing the CFD test cases along with the experimental datapoints

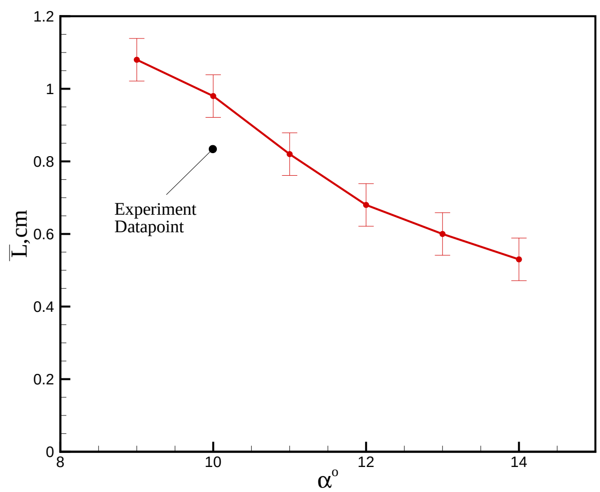

Figure 20: Variation of the windward reattachment location with angle of attack as obtained from the numerical simulations

meridian.

The change in the location of the windward attachment node with angle of attack is shown in Fig. 20. The experimental datapoint at α close to 10° is also plotted for comparison. As noted earlier the size of the separation bubble ($\overline{L}$) that is observed experimentally is smaller than the computed value. There are several reasons for this discrepancy. Most notably, the flow in the recirculation bubble is unsteady. Although majority of the unsteadiness is confined to the leeward side of afterbody there is a noticeable effect on the windward meridian. The attachment point on the windward meridian is found to oscillate about a mean location with an amplitude of upto 10% of the afterbody slant length. This uncertainty in identifying the attachment node location is denoted by an error bar in Fig. 20. The experimentally reported value of the reattachment location is based on a shadowgraph image corresponding to a single time realization of the unsteady flowfield. By comparison the computed result is based on the time-averaged solution. The comparison between CFD and experiments is improved when the uncertainty due to flow unsteadiness is taken into account in terms of the error bars. The experimental data may have additional uncertainty due to a variation in the freestream flow. The angle of attack of the projectile may oscillate it flies down the tube, thus resulting in time varying freestream conditions. The simulations consider a steady freestream at the conditions prescribed and therefore neglect any effect that the unsteady orientation of the freestream flow may have on the afterbody flowfield.

The numerical solutions can be prone to discretization error. The afterbody flowfield is usually found to be very sensitive to the quality of computation grid. Care has been taken in designing the grid so as to achieve high grid-point density in regions of high flow gradient. The gridlines are also tailored such that they are aligned to the prominent flow features like the free shear layer, the recompression shock and the wake. A limited number of grid refinements have also been performed for the baseline case of $\alpha = 10°$. The windward reattachment node location is found to be relatively insensitive to the variations in computational grid. The solutions obtained on different grids yield reattachment location within $\pm 2\%$ of that reported above. The numerical solution may also depend on the geometric modeling of the shoulder. As noted earlier a corner radius much smaller than the body dimensions is used in the current work. In the absence of specific information on the shoulder geometry in the original reference, a systematic variation of the corner radius may be used to compute the flow and to study its effect on the windward reattachment. Further the flow in the near wake may transition to turbulence. The current simulations assume laminar flow. A study of the effect of transition or turbulence on the afterbody flow features is beyond scope of the current work.

V Conclusion

We study the flow behind an Apollo-shaped body at fixed Mach number and different angles of attack. The simulations reproduce the experimentally observed afterbody flowfield, namely a large recirculation bubble on the leeward side and a small localized separation region along the windward meridian. Experiments of Kruse *et al.*[4] show that the size of the windward separation bubble decreases with increasing angle of attack. The simulations reproduce this effect and match the experimentally reported location of the reattachment point well. Further, the simulations show that the spanwise extent of the windward separation bubble increases with angle of attack. The afterbody flowfield is found to be unsteady and time-averaged solutions are computed to study the three-dimensional flow structure in the near wake and its effect on the surface properties. Surface streamlines plotted on the afterbody show a complex flow pattern with several regions of local flow separation and attachment. Most notably there are two nodes of attachment on the leeward afterbody at low angles of attack. Flow impingement at these locations result in high heat transfer to the surface. On the windward side attached flow on the later part of the afterbody frustum results in high surface heating for all the angle of attack cases studied in this work.

Acknowledgment

The authors thank the Indian Space Research Organization(ISRO) for supporting this research under the RESPOND Programme.

References

[1] Wright, M.J., Milos, F.S., and Tran, P., "Afterbody Aeroheating Flight Data for Planetary Probe Thermal Protection System Design," *Journal of Spacecraft and Rockets*, Vol. 43, No. 5, September-October 2006, pp. 929-943.

[2] Reddy, D.S.K., and Sinha, K., "Hypersonic Turbulent Flow Simulation of FIRE II Reentry Vehicle Afrerbody," *Journal of Spacecraft and Rockets*, Vol. 46, No. 4, July-August 2009, pp.745-757.

[3] Schneider, S.P., "Laminar-Turbulent Transition on Reentry Capsules and Planetary Probes," *Journal of Spacecraft and Rockets*, Vol. 43, No. 6, November-December 2006, pp. 1153-1173.

[4] Kruse, R.L, "Transition and Flow Reattchment Behind an Apollo-like Body at Mach Numbers to 9," NASA TN D-4645, 1968.

[5] MacCormack, R.W., and Candler, G.V., "The Solution of the Navier-Stokes Equations Using Gauss-Siedel Line Relaxation," *Computers and Fluids*, Vol. 17, No. 1, 1989, pp. 135-150.

[6] Sinha, K., and Candler, G.V., "Convergence Improvement of Two-equation Model Calculations," AIAA Paper 98-2649, 1998.

[7] Martin, M.P and Candler, G.V., "A Parallel Implicit Method for the Direct Numerical Simulation of Wall-bounded Compressible Turbulence," *Journal of Computational Physics*, Vol. 215, No. 1, 2006, pp 153-171.

[8] Sinha, K., and Candler, G.V., "Grid Sensitivity of Detached Eddy Simulation of a Mach 16 Re-Entry Configuration," AIAA Paper 2007-1115, 2007.

[9] Sinha, K., "Effect of Reynolds Number on Detached Eddy Simulation of Hypersonic Base Flows," AIAA Paper 2007-1457, 2007.